Droplet dynamics in Burgers vortices. I. Mass transport

Orr Avni and Yuval Dagan*
Faculty of Aerospace Engineering, Technion—Israel Institute of Technology, Haifa 320003, Israel

(Received 14 December 2022; accepted 3 April 2023; published 30 August 2023; corrected 8 October 2024)

The present series of papers studies the coupling between transport phenomena and the dynamic response of droplets in vortical flows. We derive the nonlinear relations between the vortical flow field, droplet relaxation time, drag forces, and transport phenomena and analyze the dynamics using a Lagrangian particle tracking method. The present work, paper I of the series, aims to obtain a more thorough understanding of the role of mass transport and phase change in the dynamics of droplets in the presence of Burgers vortices. Such an analytically described flow structure serves here as a model that may capture the essence of turbulent flows. Our theoretical study highlights the role of three dimensionless parameters, i.e., the vortex Euler number, the vortex Reynolds number, and the droplet initial Stokes number, characterizing the droplet transport phenomena in the vicinity of Burgers vortices. Under certain thermodynamic and hydrodynamic conditions, droplets may undergo evaporation and condensation when circulating the vortex core due to sharp changes in the environmental conditions induced by the vortex. The thermodynamic gradients give rise to complex dynamics. Droplets may stabilize around the vortex, revealing a periodic solution that emerges only when the pressure drop is high enough to generate a condensation core. This periodic behavior of the dynamic system may suggest droplet clustering induced by phase change, while the emergence of the condensation region reveals a distinct bifurcation point. Furthermore, the response of solid particles significantly differs from the droplets' response; mass transport to and from the droplets inevitably alters their trajectories relative to particles. The model derived here suggests a distinctive outlook on the role of mass transport in governing the dynamic response of droplets in vortical flow; the following paper in the series [O. Avni and Y. Dagan, following paper, Droplet dynamics in Burgers vortices. II. Heat transfer, Phys. Rev. Fluids **8**, 083605 (2023)] focuses on the role of heat transfer in the equilibrium and transient response of droplet-vortex systems.

DOI: 10.1103/PhysRevFluids.8.083604

I. INTRODUCTION

The interaction between droplets and vortical flows is a complex multiphase problem, as droplets may be influenced by laminar and turbulent flow structures spanning a wide range of scales [1,2]. The scope of any general analysis is confined by nonlinear coupling between the carrier flow and the transport of mass, momentum, and heat to the phase-changing droplet. The analysis of such multiphase flows using high-fidelity simulations may require the implementation of Lagrangian particle tracking [3–6]. However, incorporating a detailed model might require high computational costs, even for relatively simple setups. Nevertheless, some computational studies [7–11] demonstrated nonintuitive droplet dynamics within vortices, including enhanced settling distances and clustering due to droplet evaporation and condensation.

*yuvalda@technion.ac.il

On the other hand, using simplified theoretical flow models, one may employ Lagrangian methods to track the particle and droplet trajectories and estimate their dispersion [12–16] and entrapment within coherent flow structures [16–20]. Taking such an approach allows the isolation of specific transport mechanisms, including Brownian motion [21], oscillatory flows [22–24], aerosol formation [25], and particle structures [26], while studying their influence on the particle dynamics.

Among the aforementioned theoretical studies, the work of Marcu *et al.* [17] draws particular interest. They resolved the dynamics of solid particles in the vicinity of an analytically described Burgers vortex and found distinct periodic equilibrium trajectories by employing a linear stability analysis. As an exact solution of the Navier-Stokes equation, the Burgers vortex may serve as a flow model that constitutes the essence of vortical turbulent flow structures. However, the study of Marcu *et al.* [17] concerned solid particles and thus did not incorporate mass transport to the particle and its coupling to the thermodynamic gradients induced by the flow. Specifically, the shift from droplet evaporation to condensation and even freezing may be induced by intense vortices and inherently alter the droplet's transport characteristics.

In the present series of papers, we revisit the original framework of Marcu *et al.* [17] to uncover the underlying physical mechanisms governing the dynamics of droplets within vortical structures. The effect of transport phenomena on the motion of liquid droplets is studied by tracking the Lagrangian particle properties in the vicinity of an analytically described Burgers vortex; moreover, we compare it to the response of solid particles under similar flow conditions. In the present paper we isolate the influence of mass transport mechanisms on droplet dynamics. The following paper in the series [27], henceforth referred to as paper II, builds upon foundations laid here and studies the fundamental role of heat transfer processes on droplet dynamics in the vicinity of Burgers vortices.

A mathematical formulation for the carrier flow and the Lagrangian model is presented in Sec. II. In Sec. III we analyze the thermodynamics of Burgers vortices and find the parameters influencing the onset and characteristics of a condensation core that may occur within them. Section IV presents the dynamics of droplets circulating such condensation cores. The droplets' trajectories and diameters are analyzed and studied for various thermodynamic and flow properties. The model reveals essential features common to multiphase vortex flows, including the possible clustering of droplets around the vortex condensation core. The results obtained for droplets are compared to the behavior of solid nonevaporating particles under similar conditions in Sec. V. The implications and outlook of the present analysis are discussed in Sec. VI.

II. GOVERNING EQUATIONS

The transport of discrete micron-size droplets within a steady, analytically described Burgers vortex is analyzed here using a Lagrangian approach. The single droplet's spatial location $\bar{x}_p$, velocity $\bar{u}_p$, and diameter d_p are traced and coupled to the local flow $\bar{u}_f$, pressure p_f, and temperature T_f fields. We assume the droplets are dispersed and dilute enough such that their motion does not affect the flow field; furthermore, any potential interactions between droplets are discounted. The equations for the carrier flow and the Lagrangian droplet are presented in the following sections.

A. Carrier flow

The investigated carrier flow, i.e., the well-known Burgers vortex, describes an axisymmetric vortical structure under constant axial strain rate σ [28,29]. The velocity field of such flow may be expressed in cylindrical coordinates as

$$\tilde{u}_{f,r} = -\sigma\tilde{r}, \quad \tilde{u}_{f,\theta} = \frac{\Gamma}{2\pi\tilde{r}}\left[1 - \exp\left(-\frac{\sigma\tilde{r}^2}{2\nu_f}\right)\right], \quad \tilde{u}_{f,z} = 2\sigma\tilde{z}, \tag{1}$$

where Γ is the vortex circulation and ν_f is the fluid kinematic viscosity. The viscous decay and axial strain opposing effects give rise to a distinctive vortex viscous core of size $\delta = \sqrt{\nu_f/\sigma}$. We set δ as the characteristic length and $1/\sigma$ as the characteristic timescale and define the vortex Reynolds

number $\mathrm{Re}_v = \Gamma/2\pi\nu_f$. Hence, Eq. (1) may be written in a nondimensional form as

$$u_{f,r} = -r, \quad u_{f,\theta} = \frac{\mathrm{Re}_v}{r}\left[1 - \exp\left(-\frac{1}{2}r^2\right)\right], \quad u_{f,z} = 2z. \tag{2}$$

By introducing Eq. (2) into the Navier-Stokes equations, we may derive the fluid's pressure variation due to the vortical flow (see the Appendix)

$$\nabla p_f = \frac{\rho_f \sigma \nu_f}{p_0}\left[\left(\frac{u_{f,\theta}^2}{r} - u_{f,r}\frac{du_{f,r}}{dr}\right)\bar{e}_r + \left(\frac{d^2u_{f,\theta}}{dr^2} + \frac{1 - ru_{f,r}}{r}\frac{du_{f,\theta}}{dr} - \frac{1 + ru_{f,r}}{r^2}u_{f,\theta}\right)\bar{e}_\theta - \left(u_{f,z}\frac{du_{f,z}}{dz}\right)\bar{e}_z\right] \tag{3}$$

normalized with respect to the pressure at the origin p_0, the stagnation pressure. Notably, the tangential component zeros as the acceleration and viscous terms cancel each other. Integration of Eq. (3) from the origin to the abscissa (r, z), while using the exponential integral $\mathrm{Ei}(x) = \int_{-x}^{\infty} e^{-\xi}/\xi \, d\xi$ notation, yields

$$p_f = 1 - \frac{\rho_f \sigma \nu_f}{2p_0}\left[\overbrace{r^2 + (2z)^2 + \left(\frac{\mathrm{Re}_v}{r}\left[1 - \exp\left(-\frac{1}{2}r^2\right)\right]\right)^2}^{\Delta p_1} + \overbrace{\mathrm{Re}_v^2\left[\mathrm{Ei}\left(-\frac{1}{2}r^2\right) - \mathrm{Ei}(-r^2) + \ln 2\right]}^{\Delta p_2}\right]. \tag{4}$$

One may note two distinct contributions to the pressure field: the ideal inviscid pressure term $\Delta p_1 = \frac{1}{2}\rho|\bar{u}_f|^2$ and the modulation to Bernoulli's equation due to viscous effects Δp_2. We investigate the droplets' dynamics near a vortical structure, and thus we may state that $r, z \ll \mathrm{Re}_v$, i.e., we assume the pressure changes are induced only by the circulation. Under such an approximation, Eq. (4) simplifies to

$$p_f = 1 - \mathrm{Eu}\left[\left(\frac{1 - \exp\left(-\frac{1}{2}r^2\right)}{r}\right)^2 + \mathrm{Ei}\left(-\frac{1}{2}r^2\right) - \mathrm{Ei}(-r^2) + \ln 2\right], \tag{5}$$

where

$$\mathrm{Eu} = \frac{\rho_f \sigma \nu_f \mathrm{Re}_v^2}{2p_0} \tag{6}$$

is the nondimensional vortex Euler number, signifying the ratio between the dynamic pressure drop and the stagnation pressure p_0.

The suggested formulation for the vortex Euler number combines the effects of the vortical flow (represented by Re_v) and the radial suction flow (represented by $\sigma\nu_f$) on the dynamic pressure. Figure 1 demonstrates the relation between Eu and the pressure field around Burgers vortices; an increase of Eu, by either intensive suction or circulatory flow, manifests in lowers absolute pressures at the origin of the vortex. In the next section we formulate the coupling between the Lagrangian droplet dynamics and the derived, analytically described pressure field.

B. Lagrangian equations: Momentum and mass

Maxey and Riley [30] formulated the generalized equations of motion for small particles in nonuniform unsteady flows; they considered gravity, drag, virtual mass, and the Basset history force.

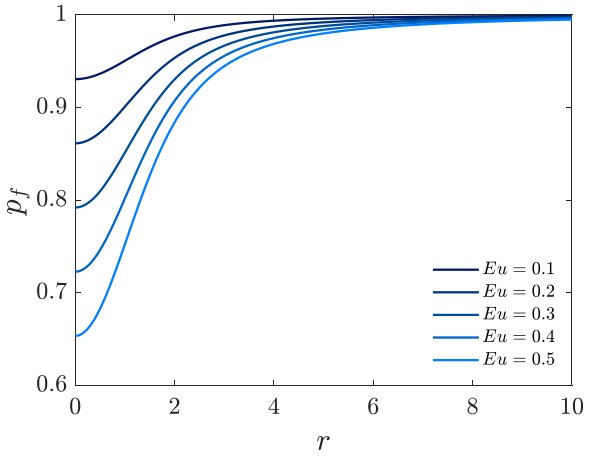

FIG. 1. Normalized pressure radial distribution $p_f(r)$ for various values of the nondimensional Euler number Eu, as predicted by Eq. (5).

This study concerns the motion of a small liquid droplet in a gaseous medium; as such, the particle-medium density ratio is large and the droplet's characteristic length is much smaller than the vortex viscous core size. Hence, we neglect the forces due to undisturbed flow, virtual mass, Faxen's drag correction, rotational inertia, and particle history terms. Additionally, we do not account for gravity and assume a linear drag term; the latter influence on the droplet dynamics is examined in paper II, while the study of gravitational effects is left for future studies. We may now reduce the general form of the equations to

$$\frac{d\bar{x}_p}{dt} = \bar{u}_p, \tag{7}$$

$$\frac{d\bar{u}_p}{dt} = \frac{\bar{u}_f - \bar{u}_p}{\mathrm{Stk}_0 d_p^2}, \tag{8}$$

where $\bar{x}_p$ and $\bar{u}_p$ are the droplet location and velocity vectors in the vortex frame of reference, respectively, d_p is the particle diameter normalized by its initial diameter, and

$$\mathrm{Stk}_0 = \frac{\tau_{p,0}}{\tau_f} = \frac{\sigma \rho_p d_0^2}{18 \nu_f \rho_f} \tag{9}$$

is the droplet initial Stokes number, i.e., the ratio between the particle's initial relaxation time and flow relaxation time.

The diameter of the Lagrangian particle is governed by mass and heat transfer processes. Kulmala *et al.* [31,32] formulated the diffusive mass transfer at the droplet-gas interface for a quasistationary case while assuming that the medium is an ideal gas, the droplet-gas interface is saturated, and a zeroth-order mass fraction profiles around the droplet. Although droplet ventilation may enhance the mass transfer out of the droplet, we aim to isolate the role of mass diffusivity and consider it as the primary transfer mechanism. In terms of droplet diameter, the mass equation is

$$\frac{d(d_p^2)}{dt} = \frac{4\rho^*_{v,\infty}}{9\,\mathrm{Sc}\,\mathrm{Stk}_0 \rho_f} \ln\left(\frac{p_f - p_{v,p}}{p_f - p_{v,\infty}}\right), \tag{10}$$

where Sc is the nondimensional Schmidt number, $\rho^*_{v,\infty}$ is the vapor ideal gas density in ambient conditions, $p_{v,p}$ is partial vapor pressure at the particle interface, and $p_{v,\infty}$ is the ambient partial vapor pressure. The difference between the vapor partial pressure at the interface and the vapor partial pressure at the far field dictates the mass flux to and from the droplet. Thus, we will estimate

both by assuming the Lagrangian particle consists of pure liquid water and the gaseous medium is an air-vapor mixture with a relative humidity of RH. We restrict the scope of our model here in order to illuminate the physical essence of the phenomena. An extended model is offered in paper II, applicable to various fluids.

The diffusive driving force in Eq. (10) takes the form

$$\frac{p_f - p_{v,p}}{p_f - p_{v,\infty}} = 1 + \frac{\mathrm{RH}p_{\mathrm{sat}}(T_0) - p_{\mathrm{sat}}(T_p)}{p_f - \mathrm{RH}p_{\mathrm{sat}}(T_0)}, \tag{11}$$

where T_p is the droplet temperature normalized with respect to the ambient temperature T_0. Let us consider that the droplet temperature is equal to the temperature of the air surrounding it $T_p \approx T_f$, i.e., the thermal relaxation time is shorter than the flow's characteristic relaxation time. This assumption eliminates the influence of heat transfer to and from the droplet, allowing one to reduce the number of independent variables and solely focus on mass transport processes. We also consider the Burgers vortex to be adiabatic; hence, one may couple the temperature field within the vortical viscous core to the pressure field thereof $T_f = (p_f)^{2/7}$, given by Eq. (5). We may now encapsulate the intricate impact of the thermodynamic properties varying due to the vortex presence into a single parameter: the mass transfer coefficient

$$C_m = \frac{\mathrm{RH}p_{\mathrm{sat}}(T_0) - p_{\mathrm{sat}}\left(p_f^{2/7}\right)}{p_f - \mathrm{RH}p_{\mathrm{sat}}(T_0)}. \tag{12}$$

The mass transfer coefficient sign and value indicate the nature of the mass transfer. Evaporation occurs when $C_m < 0$ and the droplet interface vapor pressure is higher than the far-field pressure. On the other hand, condensation occurs when $C_m > 0$ and the far-field vapor pressure is higher than the droplet interface pressure. The mass flux value is proportional to the transfer coefficient $\dot{m} \propto |C_m|$. Though relatively simple, the mass transfer coefficient will prove a powerful tool for studying the transport phenomena in the vicinity of Burgers vortices; the following section analyzes the influence of both thermodynamic conditions and vortex properties on C_m fields within it, giving rise to distinctive condensation zones.

III. CONDENSATION CORE

Both ambient thermodynamic conditions and their local variations due to the vortex presence set the mass transfer coefficient; these variations might alter the thermodynamic conditions to such an extent that the coefficient changes its sign near the vortex center. Specifically, given the right conditions, condensation initiates in the vortex viscous core, as exhibited in many natural phenomena and industrial applications. Figures 2–5 illuminate the relation between ambient and local properties to the evolving vortex condensation core. Mass transfer coefficient radial distributions at atmospheric pressure $p_0 = 1$ atm, found using Eq. (12), are analyzed for varying vortex Eu numbers, ambient air temperatures, and relative humidities. Five different C_m distributions induced by Burgers vortices of varying intensities Eu = 0.1–0.5 are presented in Fig. 2; these vortices are generated in moist air at an ambient temperature of $T_0 = 300$ K, and the relative humidity is RH = 70%. Figure 2 illustrates the role of the vortex-generated dynamic pressure drop in dictating the direction of the mass transfer. As expected, the mass transfer coefficient peaks at the center of the vortex, where the vortex-induced velocity reaches its maximum values. For Eu < 0.1, the peak mass transport coefficient $C_m(r = 0)$ is negative, i.e., the vortex is not powerful enough to generate the condensation core. However, as the vortex Euler number increases, so does the peak mass transport coefficient, resulting in a larger core and intensified condensation without any change in the far-field transport conditions. Ambient temperature effects are investigated and presented in Fig. 3; the temperature varies between $T_0 = 280$–320 K, the vortex normalized intensity is set to Eu = 0.3, and the air's relative humidity to RH = 70%. The distributions reveal that all cases share the same rudimentary characteristics: evaporation at the far field, condensation near the center of the vortex,

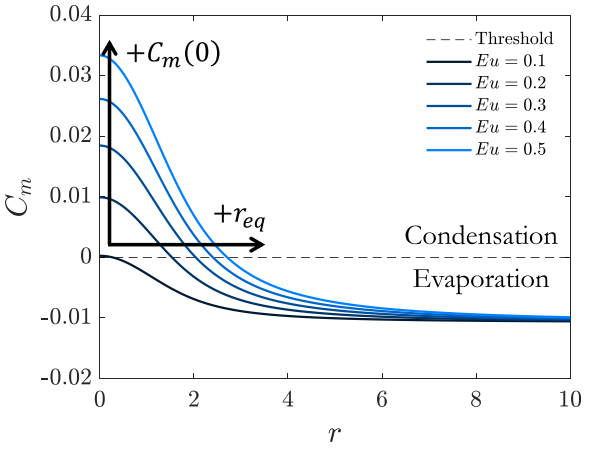

FIG. 2. Mass transport coefficient radial distributions C_m for different vortex Euler numbers Eu, ambient temperatures of $T_0 = 300$ K, and a relative humidity of RH $= 70\%$. The dashed horizontal line denotes the condensation-evaporation transition, where $C_m = 0$.

and a similar point of transition (or condensation core size) between the two. However, one may note that the transfer coefficient gradients become steeper when increasing the ambient temperature, especially near the condensation core edge. As expected, the increased temperature results in faster droplet evaporation far from the vortex, whereas the same increase, while keeping the air's relative humidity constant, leads to amplified condensation due to higher vapor mass content near and within the vortex's viscous core.

The influence of the air's relative humidity is demonstrated in Fig. 4, where different C_m radial distributions are plotted for Eu $= 0.3$, $T_0 = 300$ K, and relative humidity varying from 50% to 90%. Unlike Fig. 3, the change in relative humidity shifts the entire radial distribution, towards condensation when increased and towards evaporation when decreased, rather than altering the distribution shape itself. Higher relative humidities, for example, will result in slower evaporation at the far field, intensified condensation near the viscous core, and a larger condensation core compared to drier environments.

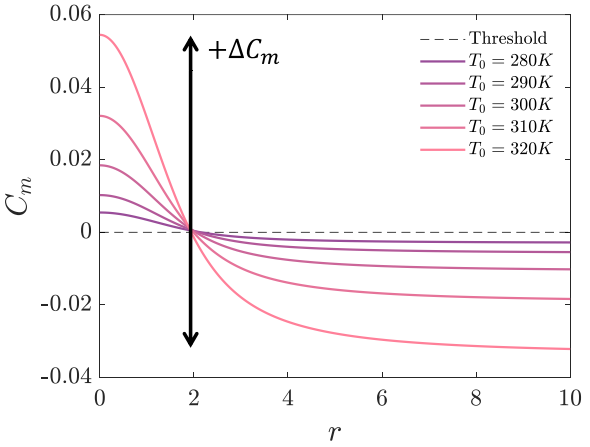

FIG. 3. Mass transport coefficient radial distributions C_m for different ambient temperatures T_0, a relative humidity of RH $= 70\%$, and a vortex Euler number of Eu $= 0.3$. The dashed horizontal line denotes the condensation-evaporation transition, where $C_m = 0$.

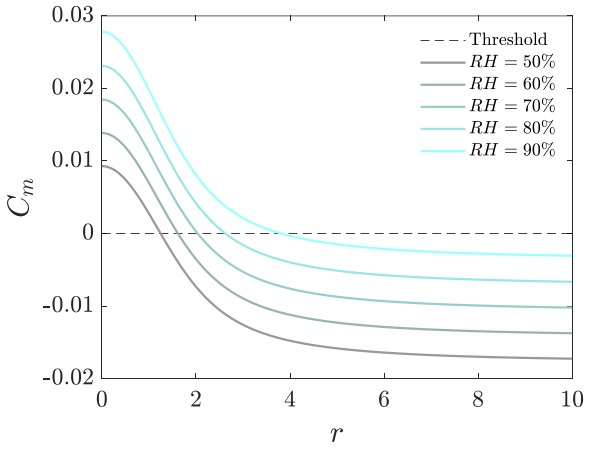

FIG. 4. Mass transport coefficient radial distributions C_m for different relative humidities RH, an ambient temperature of $T_0 = 300$ K, and a vortex Euler number of Eu $= 0.3$. The dashed horizontal line denotes the condensation-evaporation transition, where $C_m = 0$.

Figures 2 and 4 showed that both the air's relative humidity (or the vapor content within it) and the vortex intensity set the size of the vortex condensation core; their combined effect is demonstrated by Fig. 5. Here we may identify how the critical vortex Euler number, marking the onset of condensation within the vortex, changes as a function of the relative humidity: Lower humidities demand higher pressure drops inside the vortex for condensation to initiate. The condensation core quickly surpasses the viscous core ($r = 1$) in size when the intensity of the vortex is increased but remains on the scale of δ even for extreme values of Eu. Naturally, the values of the vortex Euler number are limited by physical consideration. For Eu > 1.4, the pressure at the vortex center $p_f(r = 0)$ drops below the absolute zero, an impossible thermodynamic state in gases; realistically, the vortex Euler number limit of physically possible Burgers vortices is significantly lower. Following the discussion presented on the generation of condensation cores, the following section analyzes the dynamics of Lagrangian water droplets near Burgers vortices sustaining such conditions.

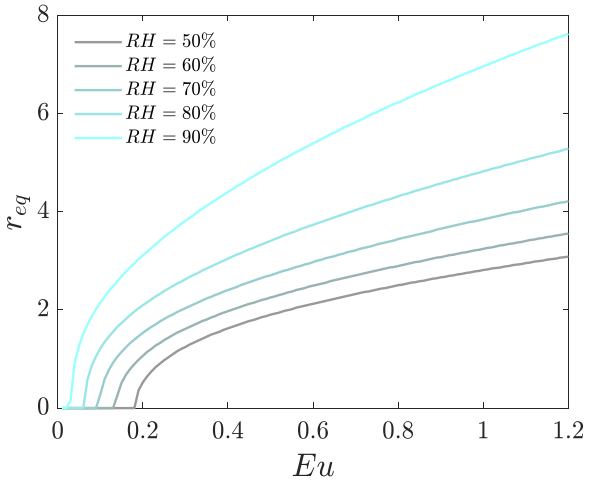

FIG. 5. Condensation core radius r_{eq} as a function of the vortex Euler number and the air relative humidity.

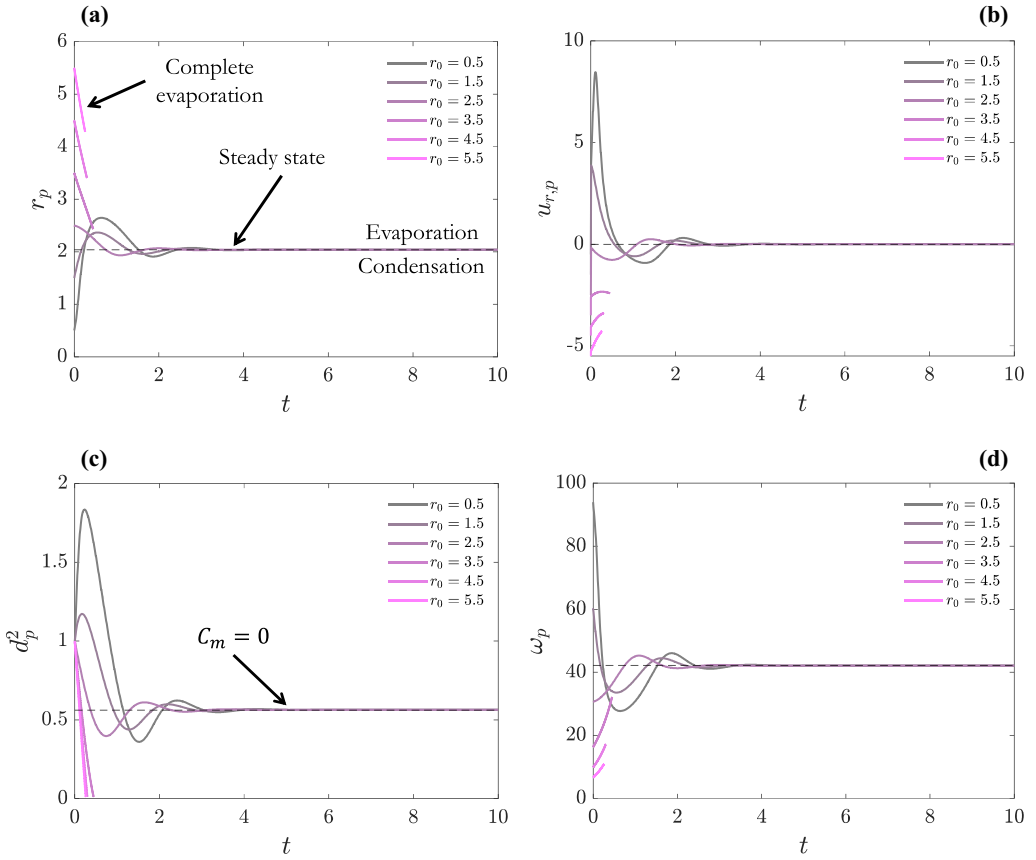

FIG. 6. (a) Radial locations, (b) radial velocities, (c) diameters, and (d) angular velocities of water droplets as a function of time. The droplets had an initial Stokes number of $\mathrm{Stk}_0 = 0.01$ and are placed at different radial locations r_0 relative to the center of a $\mathrm{Re}_v = 200$ and $\mathrm{Eu} = 0.3$ Burgers vortex. The black dashed line denotes the equilibrium state in each of the panels: (a) equilibrium trajectory around the condensation core, (b) zero radial velocity, (c) equilibrium diameter, and (d) steady-state rotation frequency.

IV. DROPLET DYNAMICS

Since we seek to study the dynamics of water droplets near Burgers vortices wherein condensation cores are forming, the air's thermodynamic properties are fixed at $p_0 = 1$ atm, $T_0 = 300$ K, and RH $= 70\%$, while we change only the droplet's (initial location Stk_0) and vortex (Eu and Re_v) properties. Each droplet is placed at a radial location $x_{p,0} = r_0$ relative to the vortex center; due to the problem's radial symmetry, the droplet's tangential location does not influence its dynamics. Furthermore, a no-slip condition is assumed as the droplet's initial velocity is set equal to the local flow velocity. Finally, in order to maintain the physicality of the analysis, the computational domain is limited to $r \leqslant 10$ and the droplet diameter to 10% of its initial value; droplets crossing these thresholds are eliminated from the simulation. Far from the vortex center, the radial and axial velocities tend to infinity, while the mass equation (10) cannot capture the droplet's complete drying without imposing an arbitrary threshold over it.

A. Droplet properties

Let us begin by studying the influence of the droplet's initial conditions. Figure 6 present the dynamics of identical water droplets ($\mathrm{Stk}_0 = 0.01$) placed at different initial radial locations

$r_0 = 0.5$–5.5 relative to the center of a Burgers vortex. In this case, the vortex Euler number is $\mathrm{Eu} = 0.3$ and its Reynolds number is $\mathrm{Re}_v = 200$. All three outer droplets ($r_0 = 3.5$–5.5) exhibit similar behavior; they quickly vanish due to intense evaporation as they stray far from the center, where $C_m < 0$. Furthermore, Fig. 6(c) reveals that the outer droplets' evaporation process conforms well to the D^2 law, as $d_p^2(t)$ is a linearly decreasing function throughout the droplets' lifetime. Inversely, the inner droplets ($r_0 = 0.5$–2.5) persist and do not evaporate completely; instead, they cluster around a distinct equilibrium trajectory. The transition from condensation conditions to evaporation conditions generates this stable equilibrium. The steady trajectory [where $u_{p,r} = 0$ in Fig. 6(b)] perfectly coincides with the vortex condensation core edge r_{eq} [black dashed line in Fig. 6(a)], found numerically by solving for $C_m(r_{\mathrm{eq}}) = 0$. Figure 6(c) showcases the extent to which condensation inside the vortex alters the droplets' size; the droplets may grow up to 2 times in surface area due to condensation when inside the core. However, the added mass leads to the droplets being ejected from the condensation core as the intensified centrifugal force overcomes the vortex's strained radial flow. Once outside the core, the droplets lose mass due to evaporation and are subsequently pulled back into the condensation core, where they condense again. The droplets that did not evaporate completely exhibit the same cyclic pattern, albeit the droplet initially located outside the core ($r_0 = 2.5$) first undergoes evaporation, while the other two ($r_0 = 0.5, 1.5$) first undergo condensation.

This dynamic response results in the droplets stabilizing around the condensation core edge, where their mass and diameter remain constant. Using the obtained condensation core size r_{eq}, we may estimate the droplet rotation frequency and diameter at equilibrium by balancing the flow-induced and centrifugal forces [17]. At equilibrium, one may state that the droplet's tangential velocity $u_{p,\theta}(r_{\mathrm{eq}}) = \omega_{p,\mathrm{eq}} r_{\mathrm{eq}}$ is equal to the flow's local velocity $u_{f,\theta}(r_{\mathrm{eq}})$. Thus, the droplet's rotation frequency is

$$\omega_{p,\mathrm{eq}} = \frac{\mathrm{Re}_v[1 - \exp\left(-\frac{1}{2}r_{\mathrm{eq}}^2\right)]}{r_{\mathrm{eq}}^2} \tag{13}$$

and the equilibrium diameter, in terms of frequency, is

$$d_{p,\mathrm{eq}}^2 = \frac{u_{f,r}(r_{\mathrm{eq}})}{\mathrm{Stk}_0 \omega_{p,\mathrm{eq}}^2 r_{\mathrm{eq}}} = \left(\mathrm{Stk}_0 \omega_{p,\mathrm{eq}}^2\right)^{-1}. \tag{14}$$

We proceed and analyze how the droplets' initial diameter, or Stokes number Stk_0, affects their dynamics. In Fig. 7 we keep the vortex properties constant ($\mathrm{Eu} = 0.3$ and $\mathrm{Re}_v = 200$) and place five droplets of varying initial Stokes number $\mathrm{Stk}_0 = 0.001$–0.1 at the vortex condensation core edge. Figure 7(a) reveals that the heavier the droplet is, that is, the larger Stk_0 is, the farther it is ejected from the center, whereas other droplets are pulled back toward the vortex core as they become lighter due to evaporation. Upon reaching the vicinity of the vortex condensation core, the droplets (excluding $\mathrm{Stk}_0 = 0.032$) oscillate around its edge and subsequently relax into a steady state.

We observe that lighter droplets respond quicker and have shorter settling times, as they tend to overshoot less significantly. One droplet slightly deviates from this dynamic behavior; the $\mathrm{Stk}_0 = 0.032$ droplet overshoots out of the core and evaporates before stabilizing about the equilibrium. Figure 7(b) demonstrates the relation between the initial Stokes number and the equilibrium diameter predicted by Eq. (14); as expected, a higher Stokes number results in a smaller equilibrium diameter. Only droplets of one particular diameter could maintain mechanical equilibrium at a specific orbit around the core. Thus, the dimensional equilibrium diameter should depend on the size of the vortex condensation core alone, while the normalized equilibrium diameter d_p should vary with Stk_0, as shown by both Eq. (14) and Fig. 7(b). Since the droplet-vortex interactions are highly sensitive to the droplet properties, we will extend our analysis and study how the dynamic changes when modifying the vortex properties.

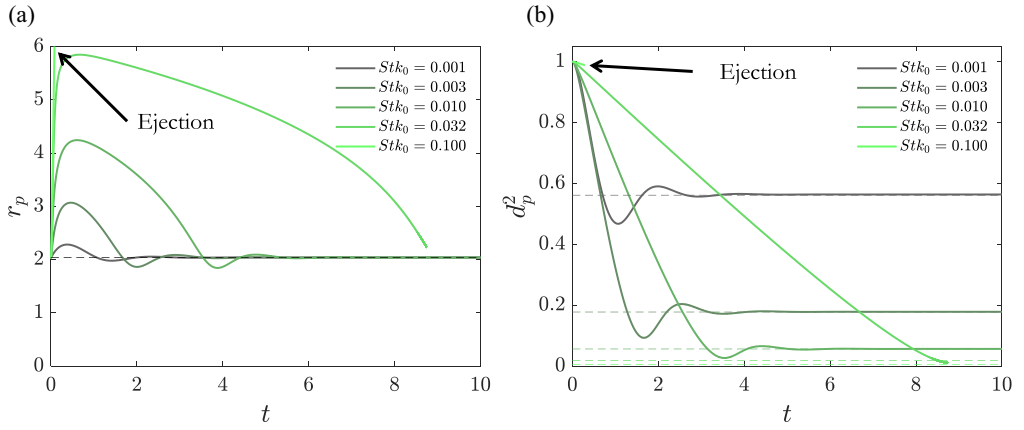

FIG. 7. (a) Radial locations and (b) diameters of water droplets as a function of time. The droplets have different initial Stokes numbers Stk_0 and are placed at the condensation core edge r_{eq} of a $\mathrm{Re}_v = 200$ and $\mathrm{Eu} = 0.3$ Burgers vortex. The dashed lines denote the equilibrium state in each panel: (a) equilibrium trajectory around the condensation core and (b) equilibrium diameters of each droplet.

B. Vortex characteristics

Here we alter the vortex characteristics and examine their influence on the radial location and diameter of identical $\mathrm{Stk}_0 = 0.01$ droplets placed at the condensation core edge r_{eq}. First, we change the normalized pressure drop and the vortex Euler number $\mathrm{Eu} = 0.1$–0.5 while keeping the vortex normalized circulation, the vortex Reynolds number, at $\mathrm{Re}_v = 200$. As exhibited in Fig. 8, the droplets are ejected to a similar radial location before being pulled back toward the center; the vortex circulation and the droplet's initial mass are constant, which leads to a roughly equal centrifugal force acting on the droplets during the initial phase. Two droplets completely evaporate while three persist; the droplets vanish when the vortex Euler number is low ($\mathrm{Eu} \leqslant 0.2$), resulting in a smaller condensation core and faster evaporation. The condensation core size decrease requires the droplets to have a longer life span to reach a steady state before completely evaporating. The droplets

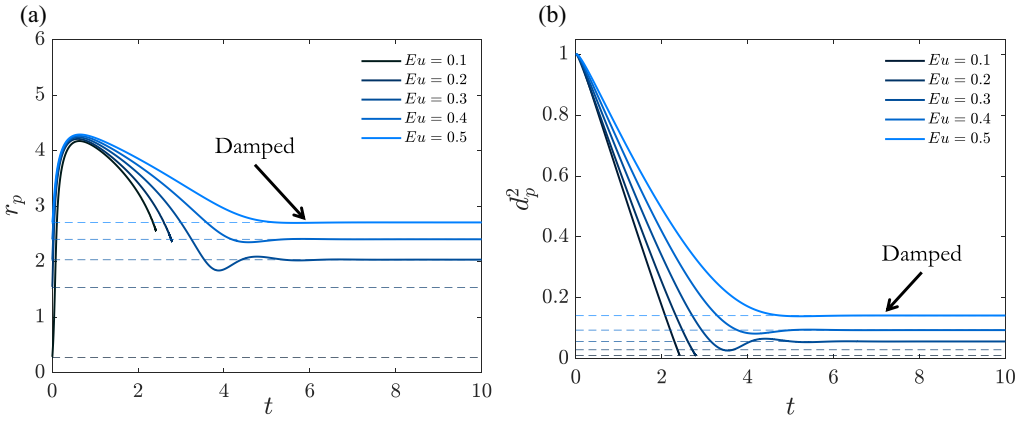

FIG. 8. (a) Radial locations and (b) diameters of water droplets as a function of time. Droplets of initial Stokes number $\mathrm{Stk}_0 = 0.01$ are placed at the condensation core edge r_{eq} of a $\mathrm{Re}_v = 200$ and varying Euler number Eu Burgers vortex. The dashed lines denote the equilibrium state in each panel: (a) equilibrium trajectories around the varying condensation core and (b) the matching equilibrium diameter.

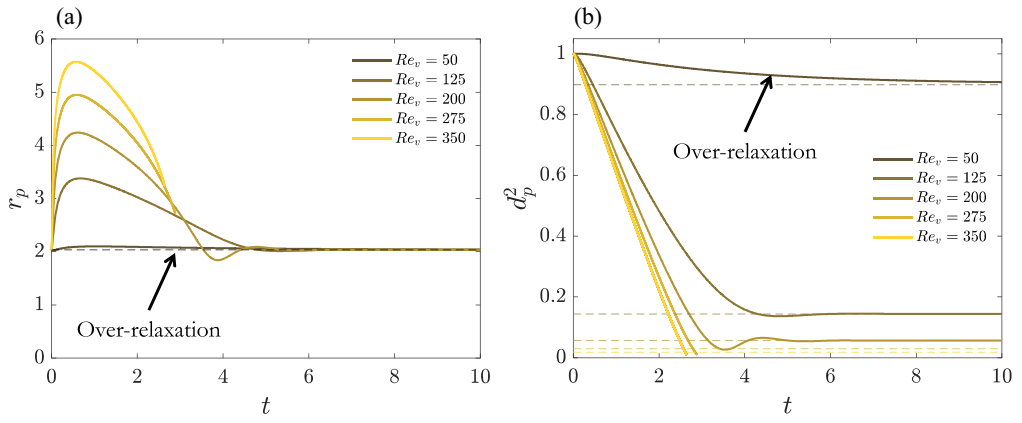

FIG. 9. (a) Radial locations and (b) diameters of water droplets as a function of time. The droplets had an initial Stokes number of $\mathrm{Stk}_0 = 0.01$ and were placed at the condensation core edge r_{eq} of a $\mathrm{Eu} = 0.3$ Burgers vortex and varying vortex Reynolds number Re_v. The dashed lines denote the equilibrium state in each panel: (a) equilibrium trajectory around the condensation core and (b) the matching equilibrium diameters.

that persist ($\mathrm{Eu} \geqslant 0.3$) stabilize at equilibrium simultaneously, i.e., they have similar relaxation times. Figure 8 shows that the highest vortex Euler number droplet $\mathrm{Eu} = 0.5$ is critically damped, relaxing into a steady state with neither position nor diameter oscillations. Contrarily, the other two droplets' radial locations and diameters are overshot, which increases when decreasing the vortex Euler number, which lowers both the equilibrium trajectory and, through the decrease in rotation frequency, the equilibrium diameter.

Figure 9 investigates the role of circulatory flow on the droplet-vortex interaction while retaining the same vortex condensation core. Here we change the vortex Reynolds number $\mathrm{Re}_v = 50$–300 while fixing the vortex Euler number at $\mathrm{Eu} = 0.3$, i.e., we alter the ratio between the strain field and circulatory flow intensity σ/Γ. Unlike Fig. 8, Fig. 9 shows that the droplets were ejected to varying radii; the higher the circulation, the farther the ejection. Once again, some droplets persist and reach equilibrium ($\mathrm{Re}_v \leqslant 200$), while others ($\mathrm{Re}_v \geqslant 300$) evaporate beforehand. The extent to which the droplets were ejected dictates whether the droplet reaches equilibrium; here droplets that surpassed $r_p > 4.5$ could not have reached the condensation core in time and have evaporated. The droplets' dynamic response changes as a function of Re_v as well: For the lowest Reynolds number $\mathrm{Re}_v = 50$ the droplet undershoots and settles to equilibrium significantly later compared to the other two slightly overshooting droplets, which have similar settling times. The vortex condensation core is kept at the same size when changing the vortex Reynolds number since the vortex Euler number remains constant. However, Fig. 9(b) shows how the equilibrium diameter changes; higher circulation dictates that in order to keep the droplets circling about the core, the mass of droplets in equilibrium should be lower despite the intensified centrifugal acceleration.

Our present analysis shows how the circulatory motion of water droplets around Burgers vortices proves a complex phenomenon, significantly influenced by the mass transfer between the droplet and the air surrounding it. We will continue by examining the dynamics of nonevaporating solid particles around Burgers vortices and compare their dynamic response to water droplets, aiming to isolate the role of mass transfer in the vortex-particle interaction.

V. COMPARISON TO NONEVAPORATING PARTICLES

As mentioned in Sec. I, the dynamics of solid particles in Burgers vortices were investigated by Marcu *et al.* [17]; they identified equilibrium points and particle trajectories both in the absence of gravity and under its influence. As done in the present study, the equilibrium trajectory was found

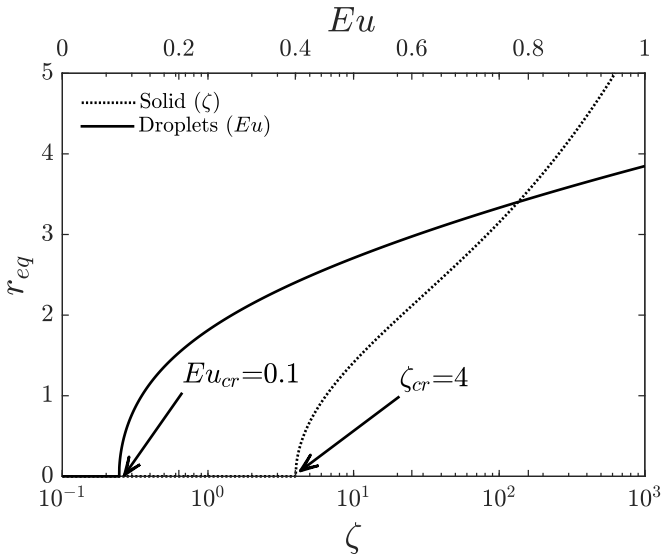

FIG. 10. Equilibrium trajectory radius for solid particles as a function of the $\zeta = \mathrm{Stk}\,\mathrm{Re}_v^2$ parameter (dotted line, lower x axis) and droplets as a function of the vortex Euler number (solid line, upper x axis) at constant relative humidity RH = 70%.

by balancing the centrifugal forces and the inward drag forces acting on the circulating particles,

$$\frac{u_{f,r}(r = r_{\mathrm{eq}})}{\mathrm{Stk}} = \omega_{p,\mathrm{eq}}^2 r_{\mathrm{eq}}, \tag{15}$$

where Stk is the particle Stokes number, similar in definition to the droplet's initial Stokes number Stk_0. The stable trajectory is given implicitly by

$$r_{\mathrm{eq}}^4 + \mathrm{Re}_v^2 \mathrm{Stk}\left[1 - \exp\left(-\frac{1}{2} r_{\mathrm{eq}}^2\right)\right] = 0, \tag{16}$$

which may be solved numerically for r_{eq}. Investigating the roots of Eq. (16), we reveal the existence of a supercritical Poincaré-Andronov-Hopf bifurcation in the dynamic system. For $\zeta = \mathrm{Re}_v^2 \mathrm{Stk} < 4$, Eq. (16) has only one real solution $r_{\mathrm{eq}} = 0$, while for $\zeta \geqslant 4$ the equation has at least one positive real root, matching the physically possible equilibrium trajectory. The value $\zeta_{\mathrm{cr}} = 4$ signifies the switch from a single stability point at the center of the vortex to a stable periodic trajectory. In physical terms, when $\zeta < \zeta_{\mathrm{cr}}$ the particle cannot maintain mechanical equilibrium around the center since the centrifugal force acting on it, due to either low inertia (small Stk) or radial velocity (small Re_v), is not high enough to overcome the vortex radial inflow, as the particle spirals towards the vortex center. When $\zeta > \zeta_{\mathrm{cr}}$, the heavier particles or higher-circulation vortices allow for increased centrifugal force, giving rise to a stable periodic solution.

This bifurcation is demonstrated in Fig. 10, where a comparison between the equilibrium trajectories' radii for particles and droplets in the same carrier medium (in our case, air) is presented. The particles' equilibrium trajectories are plotted as a function of ζ, while the droplets' trajectories are plotted as a function of Eu, assuming the air's relative humidity is constant RH = 70%. Both dynamic systems have a clear supercritical bifurcation point: $\zeta_{\mathrm{cr}} = 4$ for solid particles, as predicted by Eq. (16), and $\mathrm{Eu}_{\mathrm{cr}} = 0.1$ for droplets. However, the physical mechanism giving rise to the bifurcation is different. The existence of a condensation core generates bifurcation as the droplets stabilize around it, as discussed previously, whereas solid particles stabilize around the drag-centrifugal mechanical equilibrium trajectory. A similar periodic solution where both the

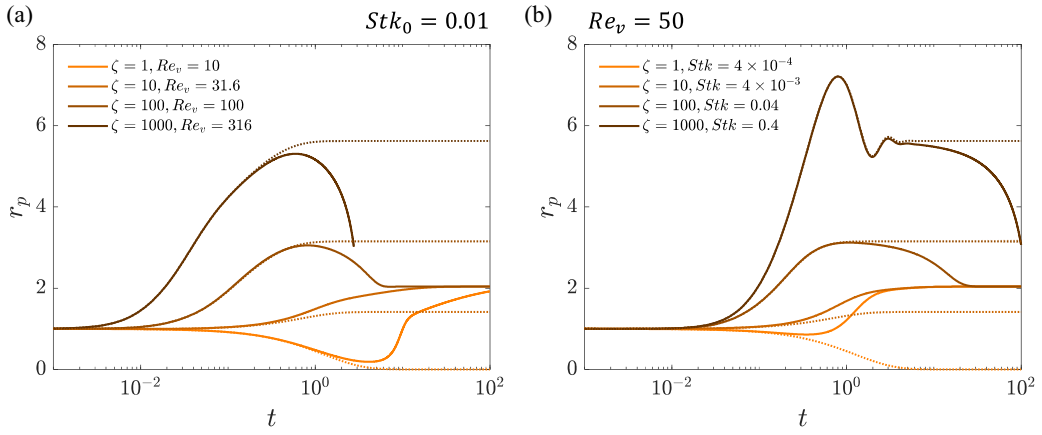

FIG. 11. Radial locations of water droplets (solid lines) and solid particles (dotted lines) as a function of time. The droplets and particles are placed at $r_0 = 1$ relative to the center of a Eu $= 0.3$ Burgers vortex. In (a) the droplets' and particles' Stokes numbers are kept constant $\mathrm{Stk}_0 = 0.01$ and the vortex Reynolds number is changed to yield different ζ parameters, while in (b) the vortex Reynolds number is constant $\mathrm{Re}_v = 50$ and the Stokes number varies.

droplets and the particles circulate the vortex arises, yet the stabilizing force driving this dynamic is entirely different.

Figure 11 compares the trajectories of droplets and particles held under the same initial conditions and in a similar Eu $= 0.3$ Burgers vortex. The nondimensional parameters Re_v and Stk are alternately fixed to set the ζ parameter (for droplets, initial ζ parameter) between $\zeta = 1$ and 1000. As revealed in Fig. 10, the solid particles' equilibrium trajectories depend only on ζ; for $\zeta < \zeta_{\mathrm{cr}}$ a stable periodic solution could not exist and the particle is pulled toward the vortex center. However, the vortex Reynolds number and the particle's Stokes number influence the particle's dynamic response. Notably, the heaviest particle [Stk $= 0.4$ in Fig. 10(b)] significantly overshoots beyond the equilibrium trajectory and oscillates around it, whereas all other particles relax into equilibrium without overshooting. The droplet's dynamics, on the other hand, do not correlate with the ζ parameter, as expected; since the vortex Euler number, and consequently the condensation core, was kept constant, the droplets clustered around it (or evaporated beforehand) regardless of their initial Stokes number or the vortex Reynolds number. The droplet trajectory diverges from the corresponding particle when mass transfer changes its mass enough to alter its dynamics; the divergence between the two is nonlinear and does not seem to correlate with a specific nondimensional number.

VI. CONCLUSION

A mathematical analysis of discrete, micron-size droplet dynamics within Burgers vortices was conducted, revealing the complex coupling between the droplet motion and the thermodynamic gradients generated by the vortex. We evaluated the pressure drop due to the vortical flow and quantified it using a nondimensional vortex Euler number Eu. The resultant gradients may be large enough to initiate condensation within the vortex core. The onset of condensation was studied by defining a mass transfer coefficient C_m, indicating the direction and extent of mass transfer to the Lagrangian water droplet. By mapping the emergence of the condensation core and its properties in moist air, we investigated the influence of ambient conditions and vortex Euler number on the mass transfer coefficient spatial distribution. The dynamics of water droplets in the vicinity of Burgers vortices was then studied for the conditions at which such condensation cores are forming; the droplets' response proved highly sensitive to the initial conditions (r_0 and Stk_0), vortex circulation

(Re_v), and pressure drop (Eu). Droplets straying from the condensation core quickly vanish due to uninterrupted evaporation in ambient air, whereas droplets in its vicinity cluster at the edge of the core. The evaporation-condensation transition allows the droplets to circulate the core periodically; they gain mass when inside the core and lose mass when ejected out, regulating the ratio between the centrifugal force and the vortex radial flow. While some droplets may oscillate around equilibrium prior to their relaxation into a steady state, others exhibit overdamping and significantly longer relaxation times. This dynamic response was affected by both the droplet and vortex properties, exhibiting the nonlinearity and coupling of the two.

Finally, we compared the trajectories of droplets and particles held under the same initial conditions. The motion of particles and droplets was significantly different, as mass transport to and from the droplets inevitably alters their trajectories relative to the particles. The particle-vortex dynamic system is known to have a supercritical bifurcation point $\zeta_{\mathrm{cr}} = \mathrm{Re}_v^2 \mathrm{Stk} = 4$, beyond which the particle can maintain stable period circulation around the vortex. The droplet-vortex system demonstrated a clear bifurcation point as well; nevertheless, the physical mechanism giving rise to the bifurcation is different. Droplets can stabilize around the vortex only when the vortex Euler number is high enough to generate a condensation core, regardless of its initial ζ parameter.

The model derived here suggests a distinctive outlook on the complex dynamic response of droplets in the vicinity of vortical flows. This approach allows the isolation of the interactions between mass transport and laminar vortex flows, which may theoretically represent the dynamics of droplets within various turbulent flow fields. This approach is extended to include mass convection and heat transfer models in paper II of this series, which focuses on the role of heat transfer in determining the equilibrium and transient response of droplet-vortex systems.

ACKNOWLEDGMENTS

This research was supported by the Israel Science Foundation (Grant No. 1762/20).

APPENDIX: PRESSURE FIELD DERIVATION

The Burgers vortex velocity field is time independent; thus, the pressure field gradient may be described as

$$\nabla \tilde{p}_f = \rho_f (\nu_f \Delta \tilde{u}_f - \tilde{u}_f \cdot \nabla \tilde{u}_f), \tag{A1}$$

and in a nondimensional form

$$\nabla p_f = \frac{\rho_f \sigma \nu_f}{p_0} (\Delta \bar{u}_f - \bar{u}_f \cdot \nabla \bar{u}_f). \tag{A2}$$

The radial and tangential velocities are a function of the radial ordinate r only, while the axial component is of the axial ordinate z. Hence, Eq. (A2) reduces to

$$\nabla p_f = \frac{\rho_f \sigma \nu_f}{p_0} \left[\left(\frac{u_{f,\theta}^2}{r} - u_{f,r} \frac{du_{f,r}}{dr} \right) \bar{e}_r + \left(\frac{d^2 u_{f,\theta}}{dr^2} + \frac{1 - r u_{f,r}}{r} \frac{du_{f,\theta}}{dr} - \frac{1 + r u_{f,r}}{r^2} u_{f,\theta} \right) \bar{e}_\theta - \left(u_{f,z} \frac{du_{f,z}}{dz} \right) \bar{e}_z \right]. \tag{A3}$$

Substituting the velocity components and their derivatives,

$$u_{f,r} = -r, \quad \frac{du_{f,r}}{dr} = -1, \tag{A4}$$

$$u_{f,z} = 2z, \quad \frac{du_{f,z}}{dz} = 2, \tag{A5}$$

$$u_{f,\theta} = \frac{\mathrm{Re}_v \exp\left(-\frac{1}{2} r^2\right)}{r} \left[-1 + \exp\left(\frac{1}{2} r^2 \right) \right], \tag{A6}$$

$$\frac{du_{f,\theta}}{dr} = \frac{\mathrm{Re}_v \exp\left(-\frac{1}{2}r^2\right)}{r^2}\left[1 + r^2 - \exp\left(\frac{1}{2}r^2\right)\right], \tag{A7}$$

$$\frac{d^2u_{f,\theta}}{dr^2} = \frac{\mathrm{Re}_v \exp\left(-\frac{1}{2}r^2\right)}{r^3}\left[-2 - r^2 - r^4 + 2\exp\left(\frac{1}{2}r^2\right)\right], \tag{A8}$$

into Eq. (A3),

$$\begin{aligned}\nabla p_f = \frac{\rho_f \sigma \nu_f}{p_0}\Bigg[&\left(-r + \frac{\mathrm{Re}_v^2}{r^2}\left[1 - 2\exp\left(-\frac{1}{2}r^2\right) + \exp(-r^2)\right]\right)\bar{e}_r \\ &+ \Bigg(\frac{\mathrm{Re}_v \exp\left(-\frac{1}{2}r^2\right)}{r^3}\Bigg\{-2 - r^2 - r^4 + 2\exp\left(\frac{1}{2}r^2\right) + (r^2+1)\left[1 + r^2 - \exp\left(\frac{1}{2}r^2\right)\right] \\ &+ (r^2-1)\left[-1 + \exp\left(\frac{1}{2}r^2\right)\right]\Bigg\}\Bigg)\bar{e}_\theta - (4z)\bar{e}_z\Bigg],\end{aligned} \tag{A9}$$

we obtain the pressure gradient in terms of the spatial location

$$\nabla p_f(r,z) = \frac{\rho_f \sigma \nu_f}{p_0}\left[\left(-r + \frac{\mathrm{Re}_v^2\left[1 - \exp\left(-\frac{1}{2}r^2\right)\right]^2}{r^3}\right)\bar{e}_r - (4z)\bar{e}_z\right]. \tag{A10}$$

We proceed to integrate Eq. (A10) from $(r = 0, z = 0)$, where $p_f = 1$, to the abscissa (r, z),

$$p_f(r,z) = 1 - \frac{\rho_f \sigma \nu_f}{2p_0}\left(r^2 + (2z)^2 - 2\,\mathrm{Re}_v^2 \int_0^r \frac{\left[1 - \exp\left(-\frac{1}{2}r^2\right)\right]^2}{r^3} dr\right). \tag{A11}$$

Using integration by parts, we further simplify the integral on the right-hand side

$$\int_0^r \frac{[1 - \exp\left(-\frac{1}{2}r^2\right)]^2}{r^3} dr = -\frac{1}{2}\frac{[1 - \exp\left(-\frac{1}{2}r^2\right)]^2}{r^2} + \frac{1}{2}\int_0^r \frac{2\exp\left(-\frac{1}{2}r^2\right) - \exp(-r^2)}{r^2} dr \tag{A12}$$

and use the exponential integral $\mathrm{Ei}(x) = \int_{-x}^{\infty} e^{-\xi}/\xi \, d\xi$ notation

$$\begin{aligned}\int_0^r \frac{2\exp\left(-\frac{1}{2}r^2\right) - \exp(-r^2)}{r^2} dr &= \int_0^\infty \frac{2\exp\left(-\frac{1}{2}r^2\right) - \exp(-r^2)}{r^2} dr \\ &\quad - \int_r^\infty \frac{2\exp\left(-\frac{1}{2}r^2\right) - \exp(-r^2)}{r^2} dr \\ &= \ln(2) + \mathrm{Ei}\left(-\frac{1}{2}r^2\right) - \mathrm{Ei}(-r^2).\end{aligned} \tag{A13}$$

Finally, Eq. (A11) yields

$$\begin{aligned}p_f = 1 - \frac{\rho_f \sigma \nu_f}{2p_0}\Bigg[&r^2 + (2z)^2 + \left(\frac{\mathrm{Re}_v}{r}\left[1 - \exp\left(-\frac{1}{2}r^2\right)\right]\right)^2 \\ &+ \mathrm{Re}_v^2\left[\mathrm{Ei}\left(-\frac{1}{2}r^2\right) - \mathrm{Ei}(-r^2) + \ln 2\right]\Bigg].\end{aligned} \tag{A14}$$

[1] D. I. Pullin and P. G. Saffman, Vortex dynamics in turbulence, Annu. Rev. Fluid Mech. **30**, 31 (1998).
[2] J. Dávila and J. C. R. Hunt, Settling of small particles near vortices and in turbulence, J. Fluid Mech. **440**, 117 (2001).
[3] S. Balachandar and J. K. Eaton, Turbulent dispersed multiphase flow, Annu. Rev. Fluid Mech. **42**, 111 (2010).
[4] G. A. Voth and A. Soldati, Anisotropic particles in turbulence, Annu. Rev. Fluid Mech. **49**, 249 (2017).
[5] M. Esmaily and A. Mani, Modal analysis of the behavior of inertial particles in turbulence subjected to stokes drag, Phys. Rev. Fluids **5**, 084303 (2020).
[6] M. Esmaily, L. Villafane, A. J. Banko, G. Iaccarino, J. K. Eaton, and A. Mani, A benchmark for particle-laden turbulent duct flow: A joint computational and experimental study, Int. J. Multiphase Flow **132**, 103410 (2020).
[7] J. Bellan and K. Harstad, The dynamics of dense and dilute clusters of drops evaporating in large, coherent vortices, Symp. (Int.) Combust. **23**, 1375 (1991).
[8] F. Fichot, K. Harstad, and J. Bellan, Unsteady evaporation and combustion of a drop cluster inside a vortex, Combust. Flame **98**, 5 (1994).
[9] K. Harstad and J. Bellan, Behavior of a polydisperse cluster of interacting drops evaporating in an inviscid vortex, Int. J. Multiphase Flow **23**, 899 (1997).
[10] K. Harstad and J. Bellan, Evaluation of commonly used assumptions for isolated and cluster heptane drops in nitrogen at all pressures, Combust. Flame **127**, 1861 (2001).
[11] S. Ghosh, J. Dávila, J. C. R. Hunt, A. Srdic, H. J. S. Fernando, and P. R. Jonas, How turbulence enhances coalescence of settling particles with applications to rain in clouds, Proc. R. Soc. A **461**, 3059 (2005).
[12] B. Marcu and E. Meiburg, Three-dimensional features of particle dispersion in a nominally plane mixing layer, Phys. Fluids **8**, 2266 (1996).
[13] B. Marcu and E. Meiburg, The effect of streamwise braid vortices on the particle dispersion in a plane mixing layer. I. Equilibrium points and their stability, Phys. Fluids **8**, 715 (1996).
[14] B. Marcu, E. Meiburg, and N. Raju, The effect of streamwise braid vortices on the particle dispersion in a plane mixing layer. II. Nonlinear particle dynamics articles you may be interested in, Phys. Fluids **8**, 734 (1996).
[15] Y. Dagan, Settling of particles in the vicinity of vortex flows, Atomization Spray. **31**, 33 (2021).
[16] O. Avni and Y. Dagan, Dynamics of evaporating respiratory droplets in the vicinity of vortex dipoles, Int. J. Multiphase Flow **148**, 103901 (2022).
[17] B. Marcu, E. Meiburg, and P. K. Newton, Dynamics of heavy particles in a Burgers vortex, Phys. Fluids **7**, 400 (1995).
[18] R. H. IJzermans and R. Hagmeijer, Accumulation of heavy particles in N-vortex flow on a disk, Phys. Fluids **18**, 063601 (2006).
[19] J.-R. Angilella, Dust trapping in vortex pairs, Physica D **239**, 1789 (2010).
[20] S. Ravichandran and R. Govindarajan, Waltz of tiny droplets and the flow they live in, Phys. Rev. Fluids **7**, 110512 (2022).
[21] N. Wang and Y. Dagan, A generalized theory of Brownian particle diffusion in shear flows, arXiv:2211.03825.
[22] Y. Dagan, J. Greenberg, and D. Katoshevski, Similarity solutions for the evolution of polydisperse droplets in vortex flows, Int. J. Multiphase Flow **97**, 1 (2017).
[23] Y. Dagan, D. Katoshevski, and J. B. Greenberg, Particle and droplet clustering in oscillatory vortical flows, Atomization Spray. **27**, 629 (2017).
[24] Y. Dagan, D. Katoshevski, and J. B. Greenberg, Similarity solutions for the evolution of unsteady spray diffusion flames in vortex flows, Combust. Sci. Technol. **190**, 1110 (2018).
[25] O. Avni and Y. Dagan, Dispersion of free-falling saliva droplets by two-dimensional vortical flows, Theor. Comput. Fluid Dyn. **36**, 993 (2022).
[26] S. R. Yerasi, R. Govindarajan, and D. Vincenzi, Spirographic motion in a vortex, Phys. Rev. Fluids **7**, 074402 (2022).
[27] O. Avni and Y. Dagan, following paper, Droplet dynamics in Burgers vortices. II. Heat transfer, Phys. Rev. Fluids **8**, 083605 (2023).

[28] J. M. Burgers, Application of a model system to illustrate some points of the statistical theory of free turbulence, Proc. R. Acad. Sci. USA **43**, 390 (1940).
[29] N. Rott, On the viscous core of a line vortex II, Z. Angew Math. Phys. **10**, 73 (1959).
[30] M. R. Maxey and J. J. Riley, Equation of motion for a small rigid sphere in a nonuniform flow, Phys. Fluids **26**, 883 (1983).
[31] M. Kulmala, A. Majerowicz, and P. E. Wagner, Condensational growth at large vapour concentration: Limits of applicability of the mason equation, J. Aerosol Sci. **20**, 1023 (1989).
[32] M. Kulmala and T. Vesala, Condensation in the continuum regime, J. Aerosol Sci. **22**, 337 (1991).

Correction: The previously published Figure 6 contained an error and has been replaced.